Modeling and Control of a Resonant Dual Active Bridge With a Tuned CLLC Network

Wynand Louis Malan, *Student Member, IEEE*, D. Mahinda Vilathgamuwa, *Senior Member, IEEE*, and Geoffrey R. Walker, *Member, IEEE*

***Abstract*—This paper proposes a linear state-space model for a phase-controlled resonant dual active bridge with a tuned capacitor–inductor–inductor–capacitor network. The proposed model is useful for fast simulation and for the estimation of state variables under large signal variation. The model is also useful for control design because the slow changing dynamics of the dq variables are relatively easy to control. Using the proposed model, a decoupled control scheme was designed which allows for the control of the high frequency link currents while also improving the soft switching range of the converter. Using steady-state relationships between state variables and the system inputs, the controller was simplified from three proportional integral (PI) controllers to a single PI controller. The controller was implemented on a low cost digital signal processor and verified experimentally. The experimental and simulation results showed the proposed model's usefulness for control design and fast simulation.**

***Index Terms*—Bidirectional converter, control design, modeling, phase control.**

I. Introduction

DUE to a rising awareness of the negative impacts that burning fossil fuels like coal and oil have on the environment, renewable energy (RE) sources are being increasingly utilized to meet our electrical energy needs. It is expected that in the next 10–20 years, the amount of electricity generated from RE sources will increase by as much as ten times [1]. Compared to the conventional way of generating electricity from RE sources in the form of large scale grid-connected wind and solar farms, distributed micro generation with its decreased transmission losses could increase the stability and power quality of the grid locally [2]. RE sources like wind and solar energy are inherently variable in their nature and this can result in mismatches between the supply and demand of electricity. To overcome this mismatch, an energy storage system such as a battery bank needs to be incorporated into the network. This requires a bidirectional power interface between the storage system and the local grid so that the battery is charged when surplus energy is being generated or the energy is extracted from the battery when there is a deficit.

Manuscript received July 19, 2015; revised October 5, 2015 and November 25, 2015; accepted November 25, 2015. Date of publication December 10, 2015; date of current version May 20, 2016. This paper was supported by the Queensland University of Technology APA scholarship. Recommended for publication by Associate Editor B. Lehman.

The authors are with the Science and Engineering Faculty, Queensland University of Technology, Brisbane, QLD 4000, Australia (e-mail: wynandlouis.malan@qut.edu.au; mahinda.vilathgamuwa@qut.edu.au; geoffrey.walker@qut.edu.au).

Color versions of one or more of the figures in this paper are available online at http://ieeexplore.ieee.org.

Digital Object Identifier 10.1109/TPEL.2015.2507787

The dual active bridge (DAB) has been offered as one of the preferred converters for bidirectional dc–dc conversion where galvanic isolation is required as it has a small number of magnetic components and modular structure. Further, its soft switching capability enables operation at high frequencies and can be operated at a wide range of voltages [3]–[5]. Much of the research surrounding the DAB converter has been related to hardware design and optimization, topology variants to improve soft switching, control strategy, and modulation schemes [6], [7].

Initially, DAB converters were operated using the single phase shift modulation strategy. This modulation scheme has received a lot of attention due to the ease of realizing soft switching when the magnitudes of the two voltages are matched by the transformer ratio. However, when the DAB converter is operated outside of this range, the converter does not operate at zero-voltage switching (ZVS) and the peak currents increase resulting in increased switching and conduction losses [5], [8]–[10]. Many other complex modulation schemes have been investigated [4], [6], [11]–[17] that have shown an improved soft switching range and lower conduction losses, however, they all still had a large reactive current at rated power.

To improve the soft switching range of the DAB various resonant dual active bridge (RDAB) topologies have been proposed [18]–[32]. The most common RDAB topology is the series RDAB (SRDAB) [21]–[27], [29]. This topology has received a lot of attention due to its low resonant network component count, only a single additional capacitor is required, and it's inherent dc blocking capability. The SRDAB is commonly modulated using a frequency modulation scheme; however, a wide switching frequency range is required to modulate the power transfer and this complicates both the control and filter design [21], [22]. Phase modulation has also been proposed for the SRDAB [24]–[27]. Corradini has shown in [27] and [24] that a minimum current trajectory can be followed when using a triple phase shift (TPS) modulation scheme. In [18] and [32], a frequency-modulated capacitor–inductor–inductor–capacitor (CLLC) RDAB is proposed that can operate over large input voltage variation while maintaining soft switching capability. The proposed CLLC RDAB can be modulated using a smaller switching frequency range compared to that of the SRDAB. In [31], a Class-E RDAB is proposed that is able to operate at high efficiency even at high switching frequencies. Additionally, due to its current sourced nature, the converter is insensitive to parasitic inductances.

Borage [33]–[36] has shown that the inductor–capacitor–inductor (LCL) resonant converter (RC) has inherent constant current characteristics when it is operated at the tuned resonant

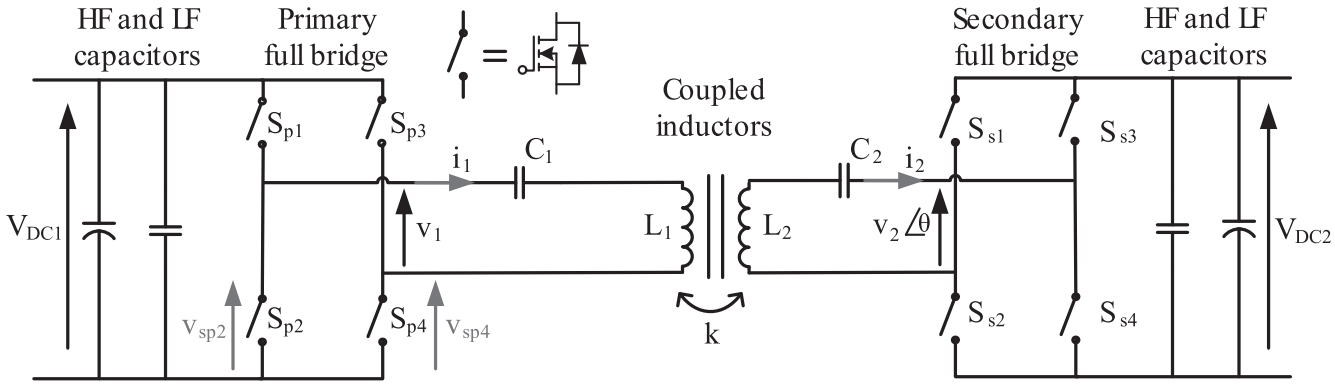

Fig. 1. Resonant dual active bridge.

frequency of the circuit. This makes the LCL RC useful for capacitor and battery charging applications. In [28] and [37], an RDAB with a tuned LCL network was proposed and it was demonstrated that the magnitude of the bridge currents were minimized when it was operated at the tuned frequency of the LCL network. This improved the switch utilization in both full bridges and also reduced the conduction losses of the high frequency link (HFL). To increase the power density of this converter, a resonant topology with a tuned CLLC structure was proposed which decreased the number of magnetic components required, decreased the required transformer magnetizing inductance and still showed similar operating characteristics to that of the LCL RDAB topology [38].

Modeling and closed-loop control of these bidirectional RCs have not yet been addressed in the literature to the authors' knowledge. The most commonly used modeling technique for pulse-width modulated dc–dc converters that directly relates the modulation signal to the output is the state-space averaging method [39]. This method assumes a small ripple, however, RCs switch at a similar frequency to the oscillatory frequency of the state-space variables, and therefore, the small ripple presumption does not hold. Various state-space modeling approaches have been utilized to model similar converters [40], [41], however, the nonlinearity of the derived models make analysis of the system and controller design difficult. To overcome this, a modeling technique was proposed which converts the ac state variables to dc values with slow dynamics by using a synchronous dq reference frame transformation [42]–[44]. This approach has been shown to be useful for the modeling of RCs under large signal variation and controller design.

The novel contributions of this paper are as follows; a linear state-space model is derived for a phase-controlled RDAB with a tuned CLLC network. This model is useful for fast simulation, estimation of state variables under large signal variation, and control design. Using the proposed model, a simplified decoupled control scheme was designed and implemented with a single PI controller that allows for control of both the primary and secondary ac current amplitudes, while ensuring soft switching of the switches.

Section II presents a brief overview of the CLLC RDAB and it is followed up with a mathematical analysis of the converter in Section III. The derivation of the proposed model is covered in Section IV and a controller is designed using the developed model in Section V. The controller was implemented on a digital signal processor (DSP) to control the prototype converter, and the experimental results are presented in Section VI.

II. Basic Operation of the RDAB

The CLLC RDAB converter, as seen in Fig. 1, consists of two full-bridge converters connected through a tuned resonant network compromising of C_1, L_1, C_2, and L_2. In this converter, the coupled inductors have a relatively low coupling factor. This results in high leakage inductances on both the primary and secondary sides of the HFL. The leakage inductances are necessary to prevent high-frequency shoot-through between the capacitors C_1 and C_2. By using coupled inductors with a low coupling factor, rather than a transformer and discrete inductors, only one magnetic component needs to be designed and manufactured which could decrease overall cost of the converter. The two series resonant LC networks are tuned as shown in (1). The capacitors C_1 and C_2 are chosen to resonate with the coupled inductors L_1 and L_2, respectively, at the switching frequency that the full bridges are operated at (ω_{sw})

$$\omega_{sw}^2 = \frac{1}{C_2 L_2} = \frac{1}{C_1 L_1}. \tag{1}$$

The two full-bridge converters are operated at a fixed frequency f_{sw} and convert the dc voltages $V_{\rm DC1}$ and $V_{\rm DC2}$ to three-level pulse-width modulated ac voltages, v_1 and v_2. The two full-bridge converters are controlled using a TPS modulation scheme as demonstrated in Fig. 2. The switches of each leg are controlled to have a duty cycle of 50% and the output of the first leg is phase shifted from the output of the second leg by ϕ_1 for the primary bridge and ϕ_2 for the secondary bridge. The output of the secondary full-bridge v_2 is phase shifted from the output of the primary full-bridge v_1, to lead v_1 by θ.

The magnitude of the power transferred has been quantified in a previous paper by the author [45] as shown in (2). It was shown that majority of the power was transferred at the fundamental frequency of the tuned resonant network

$$P = \frac{8n}{\pi^2 X_1} V_{\rm DC1} V_{\rm DC2} \sin(\theta) \sin\left(\frac{\phi_1}{2}\right) \sin\left(\frac{\phi_2}{2}\right) \tag{2}$$

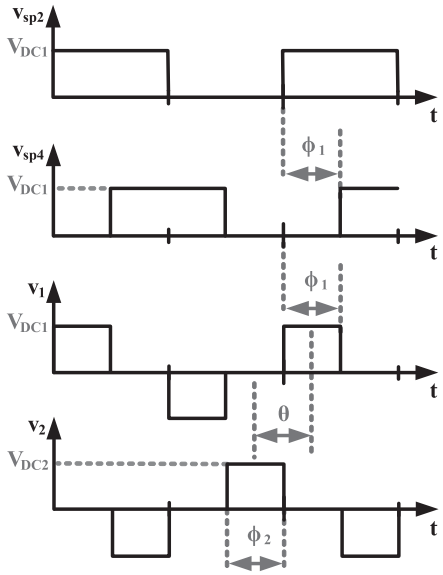

Fig. 2. TPS modulation scheme.

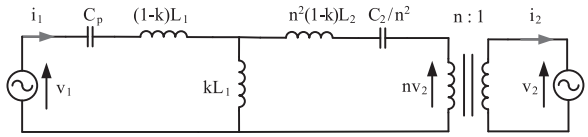

Fig. 3. Equivalent circuit at fundamental frequency.

where X_1 is

$$X_1 = \frac{1}{\omega_{sw} C_1} - \omega_{sw}(1-k)L_1 \tag{3}$$

and k is the coupling coefficient between the inductors L_1 and L_2. In (2), it is shown that the magnitude of power transferred can be controlled using ϕ_1, ϕ_2, and θ. To minimize the reactive currents at the ac terminals of the full-bridge converters, θ is usually selected as $\pm 90°$, where $+90°$ results in power flow from the primary to the secondary side and $-90°$ will cause power to be transferred from the secondary to the primary side. To control the magnitude of power transferred ϕ_1 and ϕ_2 are controlled to be between 0 and $180°$.

III. Mathematical Model

In order to simplify the mathematical analysis, the analysis will be carried out at the fundamental frequency of the resonant network f_{sw}, and the converter is assumed to be at steady state. Therefore, the converter can be simplified as shown in Fig. 3. The output of the full-bridge converters have been simplified into voltage sources, v_1 and v_2, which are represented by the Fourier series as follows:

$$v_1 = V_{DC1}\frac{4}{\pi}\sum_{a_1=1,3..}^{\infty}\frac{1}{a_1}\cos(a_1\omega_s t)\sin\left(\frac{a_1\phi_1}{2}\right) \tag{4}$$

$$v_2 = V_{DC2}\frac{4}{\pi}\sum_{a_2=1,3..}^{\infty}\frac{1}{a_2}\cos(a_2\omega_s t + a_2\theta)\sin\left(\frac{a_2\phi_2}{2}\right). \tag{5}$$

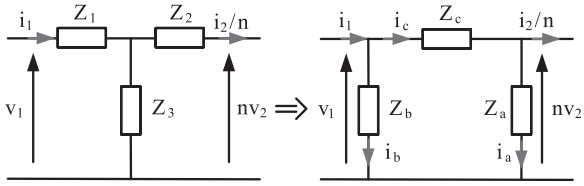

Fig. 4. Wye to delta transformation.

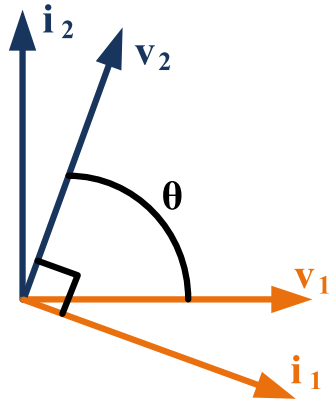

Fig. 5. Steady-state voltage and current phasors at fundamental frequency.

A. Analysis of Impedance Network

The simplified circuit model from Fig. 3 will be transformed from wye to delta. This will allow us to show the relationship between the currents, i_1 and i_2, and the voltages v_1 and v_2. The transformed equivalent circuit is shown in Fig. 4. By applying circuit equations to the delta network, one can obtain the following relationships between the voltages, v_1 and v_2, to the currents i_1 and i_2:

$$i_1 = \left(\frac{1}{Z_c} + \frac{1}{Z_b}\right)v_1 - \frac{n}{Z_c}v_2 \tag{6}$$

$$i_2 = -\left(\frac{1}{Z_c} + \frac{1}{Z_a}\right)n^2 v_2 + \frac{n}{Z_c}v_1. \tag{7}$$

Since the CLLC network is tuned to the switching frequency, we can substitute (1) into the delta impedance equations and simplify to obtain the following relationship:

$$Z_c = -Z_a = -Z_b = -j\omega_{sw} k L_1. \tag{8}$$

Substituting (8) into (6)–(7)

$$i_1 = \frac{nv_2}{j\omega_{sw} k L_1} \tag{9}$$

$$i_2 = -\frac{nv_1}{j\omega_{sw} k L_1}. \tag{10}$$

This shows that at the switching frequency and in steady-state i_1 is decoupled from v_1 and i_2 is decoupled from v_2.

The relationships between the voltages and currents in (9)–(10) are shown in Fig. 5 as a phasor diagram. The diagram shows that v_2 is fixed to lead i_1 by $90°$ and i_2 is fixed to lead v_1 by $90°$. From this, we can see that when θ is $\pm 90°$ the voltage phasors are in phase with their respective current phasor. This results in unity power factor at the ac terminals of both

full-bridge converters, which minimizes the reactive currents in the circuit and reduces both the switching and conduction losses of the converter.

B. Modulation Strategy

From (2), it is evident that the magnitude of power transferred through the RDAB can be modulated using three variables, ϕ_1, ϕ_2, and θ. How these parameters are modulated is dependent on the optimization goals of the converter. In this paper, the optimization goal is first to minimize the switching losses of the converter, so that operation at high frequency is possible, and second to minimize the conduction losses in the HFL. The switching losses are only significant when the converter is hard switching, therefore, the modulation strategy will be selected so that the converter will be soft switching over the whole power transfer range. The conduction losses are mainly due to the resonant tank parasitics in the form of equivalent series resistance (ESR). To minimize the conduction losses due to the ESRs, the HFL currents should be minimized. To investigate the effects that the modulation variables have on the current, (4) and (5) have been substituted into (9) and (10)

$$|i_1| = \frac{n4V_{\mathrm{DC2}}}{\pi\omega_{sw}kL_1}\sin\left(\frac{\phi_2}{2}\right) \tag{11}$$

$$|i_2| = -\frac{n4V_{\mathrm{DC1}}}{\omega_{sw}kL_1}\sin\left(\frac{\phi_1}{2}\right). \tag{12}$$

From (11) and (12), we can see that the magnitudes of the HFL currents i_1 and i_2 are controlled by the phase shifts ϕ_1 and ϕ_2. So the chosen modulation strategy needs to decrease ϕ_1 and ϕ_2 as the power transfer magnitude is lowered to keep the HFL currents low. In [38] and [37], θ was fixed at $\pm 90^\circ$ so that unity power factor is maintained at the outputs of the full bridges, ϕ_1 and ϕ_2 were used to control the magnitude of power transfer. At maximum power transfer, the converter is zero-current switching (ZCS) or near ZCS as shown in Fig. 6(a). However, as the magnitude of power transfer is modulated down using ϕ_1 and ϕ_2, some of the switches start hard switching as can be seen in Fig. 6(b). In this paper, soft switching is prioritized over the unity power factor operation so that the CLLC RDAB topology can be utilized in higher switching frequency applications. In order to regain soft switching at lower power transfer magnitudes, θ will be deviated from $\pm 90^\circ$ so that the previously hard switching instances will now be soft switching under ZCS conditions as shown in Fig. 6(c).

In Fig. 7, the relationships between the voltage and current waveforms and the modulation parameters can be seen. From Fig. 7(a), we can see that ϕ_1 controls the pulse width of v_1, and therefore, the magnitude of the fundamental component of v_1, while θ controls the phase difference between i_1 and v_1. In Fig. 7(b), ϕ_2 controls the pulse width of v_2 and θ controls the phase difference between i_2 and v_2. By analysis of Fig. 7, the following relationship can be found for soft switching through ZCS, rather than the hard switching that was seen earlier in Fig. 6(b)

$$\theta = \frac{\phi_1}{2} = \frac{\phi_2}{2}. \tag{13}$$

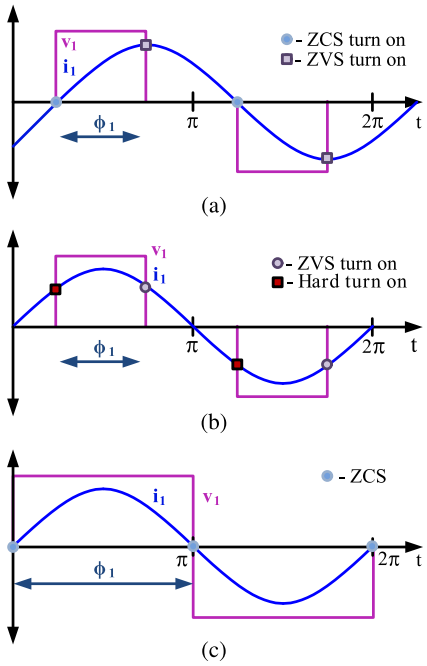

Fig. 6. Current and voltage waveforms (a) at maximum power transfer capability, (b) with modulation of ϕ_1 and ϕ_2 while θ is fixed $\pm 90^\circ$ nd (c) modulation of ϕ_1, ϕ_2, and θ.

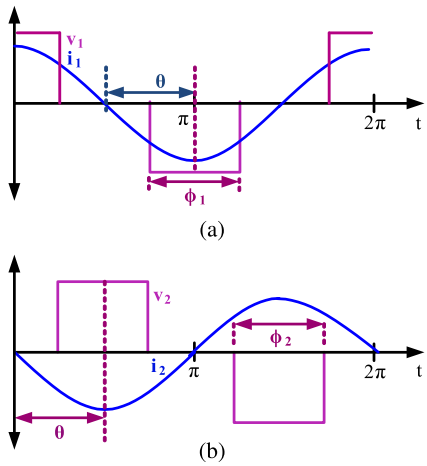

Fig. 7. Relationships between (a) primary full-bridge waveforms and modulation parameters (b) secondary full-bridge waveforms and modulation parameters.

To regain soft switching, θ has be varied according to (13), the further θ is varied from $\pm 90^\circ$, the lower the power factor at the output of the full bridges. This means that the soft switching is gained at the expense of increasing the circulating currents in the HFL. In Fig. 8, a comparison of the magnitudes of the HFL currents between the previously used and proposed modulation strategies is shown. This shows that as the power transfer magnitude is decreased, the HFL currents in the proposed strategy is slightly higher than that of the previously used strategy. A similar relationship between the conduction losses of the two modulation strategies is expected, however, the proposed modulation strategy is expected to incur lower switching losses due to improved soft switching capabilities.

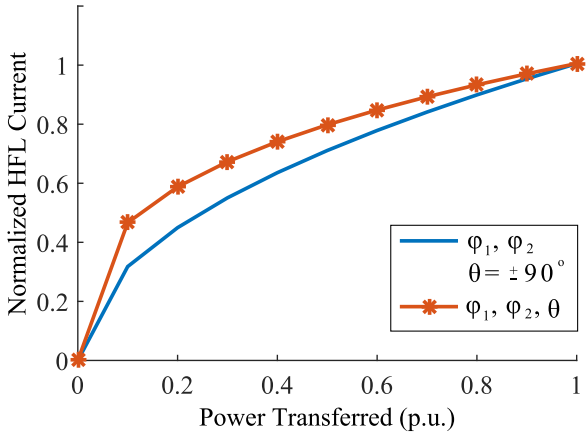

Fig. 8. Comparison of HFL current magnitudes $|i_1| + |i_2|$ between the modulation strategies.

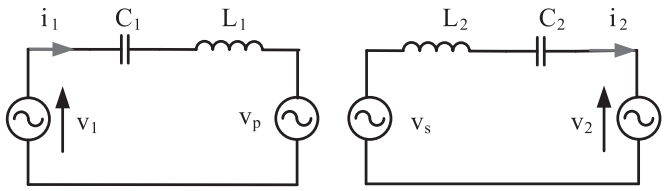

Fig. 9. Equivalent circuit of the CLLC RDAB HF ac link.

For the remainder of this study, the modulation strategy which modulates θ along with ϕ_1 and ϕ_2 will be utilized to modulate the currents in the HFL of the RDAB, and therefore, the magnitude of power transfer. This modulation strategy has been selected because it improves the soft switching range of the converter while only slightly increasing the magnitude of the currents in the HFL. The increased soft switching range is especially important for high switching frequency applications where the switching losses dominate the conduction losses.

IV. State-Space Model

A. HFL Model

The RDAB converter has two stages of conversion, an inverting stage and a rectifying stage. This results in three subsystems, a high-frequency ac subsystem and two dc subsystems. In this section, a model will be derived for the HF ac link and the controllability and interactions of the system will be analyzed. The HF ac link has been simplified into the equivalent circuit seen in Fig. 9.

The voltages v_s and v_p are the induced voltages due to the mutual inductance of the transformer and they have been defined below

$$v_p = -M\frac{di_2}{dt} \tag{14}$$

$$v_s = M\frac{di_1}{dt} \tag{15}$$

where M represents the mutual inductance between the transformer windings, L_1 and L_2, and is defined as

$$M = k\sqrt{L_1 L_2}. \tag{16}$$

From Fig. 9, we can observe that the HF ac link has four state variables; v_{c1}, v_{c2}, i_1, and i_2, and two inputs, v_1 and v_2. The system can be described by (17)–(20)

$$\frac{dv_{c1}}{dt} = \frac{1}{C_1}i_1 \tag{17}$$

$$\frac{dv_{c2}}{dt} = \frac{1}{C_2}i_2 \tag{18}$$

$$\frac{di_1}{dt} = -a_1 v_{c1} - \frac{a_1 M}{L_2}v_{c2} - a_1 R_1 i_1 - \frac{a_1 M R_2}{L_2}i_2 + a_1 v_1 - \frac{a_1 M}{L_2}v_2 \tag{19}$$

$$\frac{di_2}{dt} = -\frac{a_2 M}{L_1}v_{c1} - a_2 v_{c2} - \frac{a_2 M R_1}{L_1}i_1 - a_1 R_2 i_2 + \frac{a_2 M}{L_2}v_1 - a_2 v_2 \tag{20}$$

where a_1 and a_2 are as follows:

$$a_1 = \frac{1}{L_1 - \frac{M^2}{L_2}} \tag{21}$$

$$a_2 = \frac{1}{L_2 - \frac{M^2}{L_1}}. \tag{22}$$

R_1 and R_2 represent the ESRs of the primary and secondary transformer windings.

B. DQ Model

All of the states are periodic and can, therefore, be represented by a Fourier series. In [38], it has been shown that power transfer mainly occurs at the fundamental frequency of the tuned resonant circuit, and therefore, the modeling and analysis of the ac subsystem will be done at the fundamental frequency or ω_{sw}. Since the state variables are assumed to be sinusoidal at the fundamental frequency, the following equations can represent the ac states:

$$v_1 = v_{1d}\sin(\omega_{sw}t) + v_{1q}\cos(\omega_{sw}t) \tag{23}$$

$$v_2 = v_{2d}\sin(\omega_{sw}t) + v_{2q}\cos(\omega_{sw}t) \tag{24}$$

$$v_{c1} = v_{c1d}\sin(\omega_{sw}t) + v_{c1q}\cos(\omega_{sw}t) \tag{25}$$

$$v_{c2} = v_{c2d}\sin(\omega_{sw}t) + v_{c2q}\cos(\omega_{sw}t) \tag{26}$$

$$i_1 = i_{1d}\sin(\omega_{sw}t) + i_{1q}\cos(\omega_{sw}t) \tag{27}$$

$$i_2 = i_{2d}\sin(\omega_{sw}t) + i_{2q}\cos(\omega_{sw}t). \tag{28}$$

The amplitudes of the sinusoids are time varying Fourier coefficients. These Fourier coefficients will represent the new system states and inputs to the model. The new system equations can be found by substituting (23)–(28) into (17)–(20) and equating the sines and cosines.

The derived system equations can be represented in state-space form as follows:

$$\dot{x} = Ax + Bu \tag{29}$$

$$y = Cx + Du \tag{30}$$

$$x = \begin{bmatrix} v_{c1q} & v_{c1d} & v_{c2q} & v_{c2d} & i_{1q} & i_{1d} & i_{2q} & i_{2d} \end{bmatrix}^T \tag{31}$$

$$u = \begin{bmatrix} v_{1q} & v_{1d} & v_{2q} & v_{2d} \end{bmatrix}^T \tag{32}$$

$$A = \begin{bmatrix} 0 & -\omega & 0 & 0 & \cdots \\ \omega & 0 & 0 & 0 & \\ 0 & 0 & 0 & -\omega & \\ 0 & 0 & \omega & 0 & \\ -a_1 & 0 & -\frac{a_1 M}{L_2} & 0 & \\ 0 & -a_1 & 0 & -\frac{a_1 M}{L_2} & \\ -\frac{a_2 M}{L_1} & 0 & -a_2 & 0 & \\ 0 & -\frac{a_2 M}{L_1} & 0 & -a_2 & \end{bmatrix}$$

$$\begin{bmatrix} \frac{1}{C_1} & 0 & 0 & 0 \\ 0 & \frac{1}{C_1} & 0 & 0 \\ 0 & 0 & \frac{1}{C_2} & 0 \\ 0 & 0 & 0 & \frac{1}{C_2} \\ \cdots & & & \\ -a_1 * R_1 & -\omega & -\frac{a_1 M R_2}{L_2} & 0 \\ \omega & -a_1 R_1 & 0 & -\frac{a_1 M R_2}{L_2} \\ -\frac{a_2 M R_1}{L_1} & 0 & -a_2 R_2 & -\omega \\ 0 & -\frac{a_2 M R_1}{L_1} & \omega & -a_2 R_2 \end{bmatrix} \tag{33}$$

$$B = \begin{bmatrix} 0 & 0 & 0 & 0 & a_1 & 0 & \frac{a_2 M}{L_2} & 0 \\ 0 & 0 & 0 & 0 & 0 & a_1 & 0 & \frac{a_2 M}{L_2} \\ 0 & 0 & 0 & 0 & -\frac{a_1 M}{L_2} & 0 & -a_2 & 0 \\ 0 & 0 & 0 & 0 & 0 & -\frac{a_1 M}{L_2} & 0 & -a_2 \end{bmatrix}^T. \tag{34}$$

TABLE I
SIMULATION PARAMETERS

Parameter	Value	Parameter	Value
$V_{DC1} = V_{DC2}$	20 V	f_{sw}	50 kHz
$C_1 = C_2$	200 nF	$L_1 = L_2$	50.3 μH
$R_1 = R_2$	0.04 Ω	k	0.65

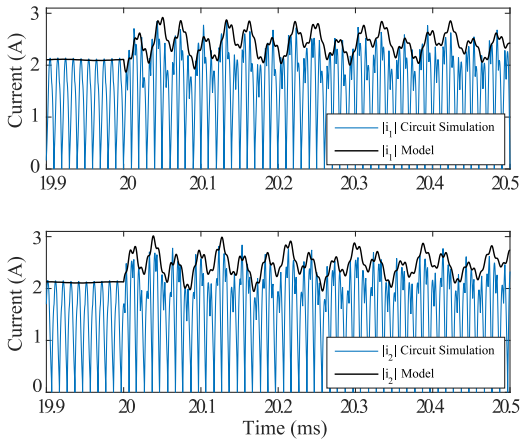

Fig. 10. Step response of circuit simulation and state-space model.

The C and D matrices have been selected so that the outputs are the current components of interest as shown in (35)

$$y = \begin{bmatrix} i_{2d} & i_{2q} & i_{1d} & i_{1q} \end{bmatrix}^T. \tag{35}$$

C. Model Validation by Simulation

A circuit simulation of the CLLC RDAB was built in MATLAB using the PLECS toolset with the parameters shown in Table I. In Fig. 10, ϕ_1 and ϕ_2 are stepped up from $2\pi/3$ to π at $t = 20$ ms, this corresponds to the equivalent step in the dq model of v_{1d} and v_{2q} from $\frac{8}{3\pi}V_{DC1}$ and $\frac{8}{3\pi}V_{DC2}$ to $\frac{4}{\pi}V_{DC1}$ and $\frac{4}{\pi}V_{DC2}$, respectively. The response from the DQ model is shown in black and the response of the circuit simulation is shown in blue. The output of the DQ model represents the fundamental Fourier coefficients and, therefore, indicate the current amplitude. The circuit simulation, however, calculates the whole current waveform. This figure shows that the dq model closely predicts the transient response of the circuit model.

To compare the steady-state response of the circuit simulation with that of the derived DQ model, the power transfer equation from (2) has been redefined as follows:

$$P = \frac{8n}{\pi^2 X_1} V_{DC1} V_{DC2} \times \text{Modulation Factor}. \tag{36}$$

where the modulation factor is

$$\text{Modulation Factor} = \sin(\theta) \sin\left(\frac{\phi_1}{2}\right) \sin\left(\frac{\phi_2}{2}\right). \tag{37}$$

The modulation factor represents the magnitude of power transfer and will be used in the comparison of the steady-state current magnitudes of the circuit simulation and the DQ model. The

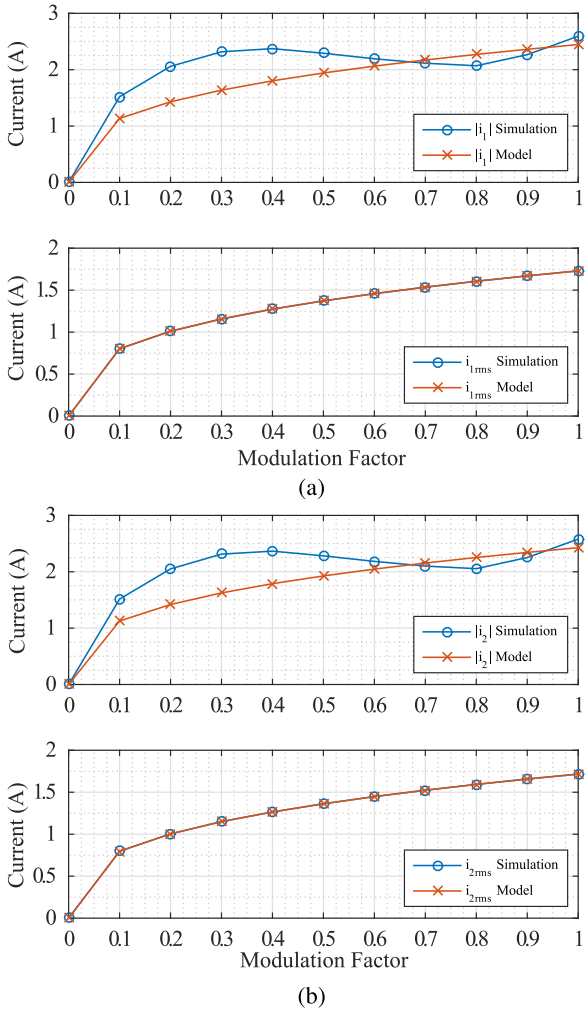

Fig. 11. Comparison of the steady-state current magnitude between the circuit simulation and state-space model for the (a) primary current and (b) secondary current.

results of this comparison can be seen in Fig. 11(a) and (b). From these figures, it's evident that the current magnitudes predicted by the DQ model have some steady-state error, most considerably when the modulation factor is low. This is due to the harmonics present in the circuit simulation which are not accounted for by the fundamental DQ model. However, we can see from these figures that even though the current magnitudes or peaks are distorted, the root mean square (RMS) values of the current waveforms match closely. This indicates that even though the current waveform magnitudes are distorted by the harmonics, the magnitude of power transfer which occurs mainly at the fundamental frequency is still well modeled by the DQ model.

V. Control Design

A. Relative-Gain-Array (RGA) Analysis

The RGA is a useful tool to analyze the degree of interaction in a multiple-input-multiple-output (MIMO) system. It was originally defined by Bristol [46] as shown below

$$\mathrm{RGA}(G)) = \Lambda(G) \triangleq G \times (G^{-1})^T. \tag{38}$$

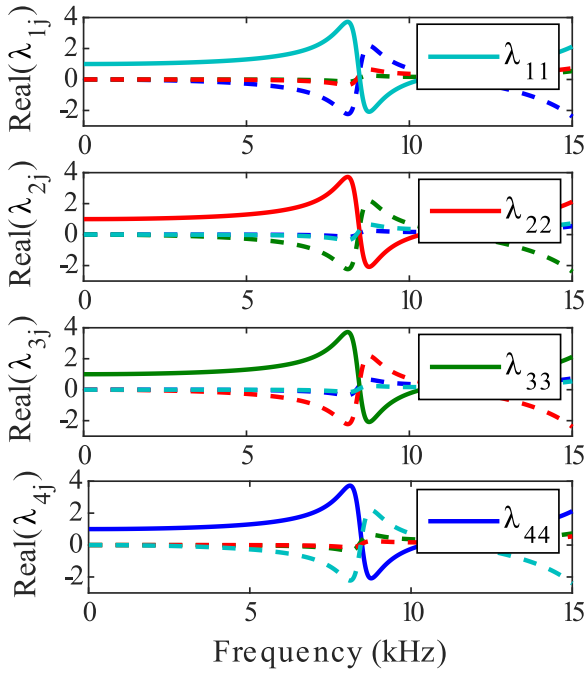

Fig. 12. RGA values of dominant input–output pairs.

If u_j and y_i denote a particular input–output pair of a MIMO system, then the relative gain λ_{ij} between the input j and output i is defined as

$$\lambda_{ij} = \frac{(\delta y_i/\delta u_j)_{u_k=0,k\neq j}}{(\delta y_i/\delta u_j)_{y_k=0,k\neq i}} \tag{39}$$

where $(\delta y_i/\delta u_j)_{u_k=0,k\neq j}$ represents the gain between input j and output i when all the other loops are open and $(\delta y_i/\delta u_j)_{y_k=0,k\neq i}$ represents the gain when all the other loops are closed. The elements of the RGA provide information on the interaction between a particular input and output of the system. A large value indicates strong interaction and a low value represents weak interaction. Since the gain of the system (G) is frequency dependent, the RGA has been calculated over a large range of frequencies and the results have been plotted in Fig. 12. Since we are using the dq model which models the ac states as the dc values with slow dynamics, the operating frequency we are interested in is dc. The RGA at this operating point is as follows:

$$|\Lambda(0)| = \begin{bmatrix} 0.9993 & 0.0002 & 0 & 0.0004 \\ 0.0002 & 0.9993 & 0.0004 & 0 \\ 0 & 0.004 & 0.9993 & 0.0002 \\ 0.0004 & 0 & 0.0002 & 0.9993 \end{bmatrix}. \tag{40}$$

It can be seen that at this operating point there is strong interaction between; u_1 and y_1, u_2 and y_2, u_3 and y_3, and between u_4 and y_4. The RGA values for the other input–output pairs indicate very little to no interaction at this frequency. This shows that the system is diagonally dominant and, therefore, a decoupled control scheme could be employed.

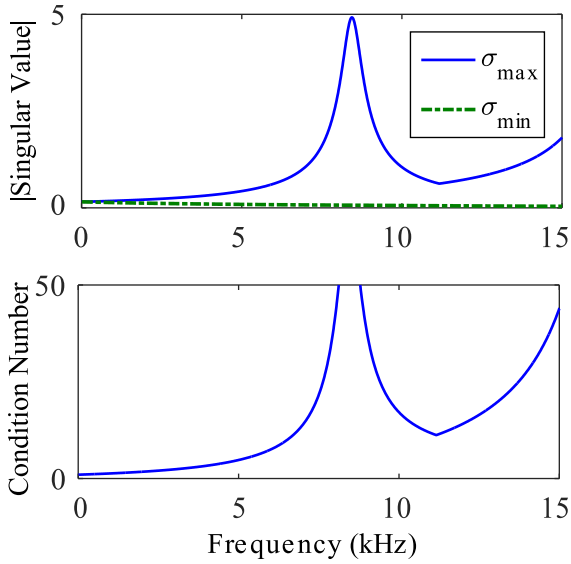

Fig. 13. SVD and the condition number of the system.

B. Singular Value Analysis

The eigenvalues of a transfer function matrix (G) in a MIMO system does not provide any meaningful information, unlike for a single-input single-output system (SISO) system. One of the most useful parameters to analyze for a MIMO system is the singular values [47]. The singular values are the positive square roots of the eigenvalues of $G^H G$, where G^H is the complex conjugate transpose of G

$$\sigma_i(G) = \sqrt{\lambda_i(G^H G)}. \tag{41}$$

The singular values of the system are functions of frequency. To analyze the performance of the system, the condition number will be used. The condition number is defined as

$$\gamma(G) \triangleq \frac{\bar{\sigma}}{\underline{\sigma}} \tag{42}$$

where $\bar{\sigma}$ is the maximum singular value and $\underline{\sigma}$ is the minimum singular value. The maximum and minimum singular values have been plotted in Fig. 13 as well as the condition number over a wide range of frequencies. The condition number has been calculated below for the operating point of the converter and has been identified as 1.003.

As the condition number is low, this indicates that the multivariable effects of uncertainty are not likely to be serious [47].

C. Decentralized Control Scheme

The focus of this paper is to control the amplitudes of the currents in the resonant tank, i_1 and i_2, while ensuring soft switching of the switches by modulating θ. As mentioned in an earlier section, θ will be varied so that the soft switching range of the converter can be improved, while ϕ_1 and ϕ_2 are varied to control the magnitudes of the currents i_1 and i_2. This results in a system with three degrees of freedom namely ϕ_1, ϕ_2, and θ. The magnitude of the input variables v_{1d}, v_{1q}, v_{2d}, v_{2q} have the

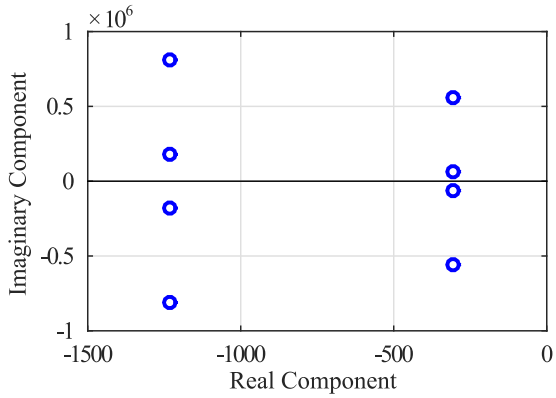

Fig. 14. Open-loop poles of the transfer function from input v_{1d} to output i_{2q}.

relationships to ϕ_1, ϕ_2, V_{DC1}, and V_{DC2} shown in (43)–(47). v_{1q} is zero because v_{1d} was selected to be the reference for our dq frame

$$v_{1d} = \frac{4}{\pi} V_{\mathrm{DC1}} \sin\left(\frac{\phi_1}{2}\right) \tag{43}$$

$$v_{1q} = 0 \tag{44}$$

$$v_{2q} = \frac{4}{\pi} V_{\mathrm{DC2}} \sin\left(\frac{\phi_1}{2}\right) \sin(\theta) \tag{45}$$

$$v_{2d} = \frac{4}{\pi} V_{\mathrm{DC2}} \sin\left(\frac{\phi_1}{2}\right) \cos(\theta) \qquad \text{for } \theta \geq 0 \tag{46}$$

$$= \frac{-4}{\pi} V_{\mathrm{DC2}} \sin\left(\frac{\phi_1}{2}\right) \cos(\theta) \qquad \text{for } \theta < 0. \tag{47}$$

Since our system is very strongly diagonally dominant, we can assume that every input will affect only its corresponding diagonal output. Since v_{1q} is zero due to the selection of v_{1d} as our reference frame and i_{2d} is solely affected by v_{1q}, we can assume that i_{2d} will also be zero. Therefore, the magnitude of i_1 and i_2 can be derived as follows:

$$i_{2d} = 0 \tag{48}$$

$$|i_2| = \sqrt{i_{2d}^2 + i_{2q}^2}$$

$$= i_{2q} \tag{49}$$

$$|i_1| = \sqrt{i_{1d}^2 + i_{1q}^2}. \tag{50}$$

Since a decentralized control scheme will be employed, an independent design approach can be taken to design the controllers for i_{1q}, i_{1d}, and i_{2q}. This allows independent design of the control loops using the diagonal elements of G(s). To design the first PI controller, the transfer function from input v_{1d} to output i_{2q} will be used. The transfer function of this loop, for a converter with the parameters shown in Table I, was calculated in MATLAB and the poles have been plotted in Fig. 14. Since all the poles are on the left side of the imaginary axis, we know that this loop is stable.

A bode plot of this transfer function can be seen in Fig. 15. From this bode plot, we can see that the system is stable at lower

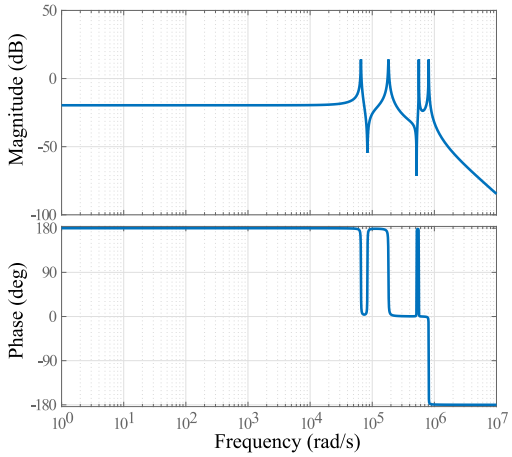

Fig. 15. Bode plot of open-loop system.

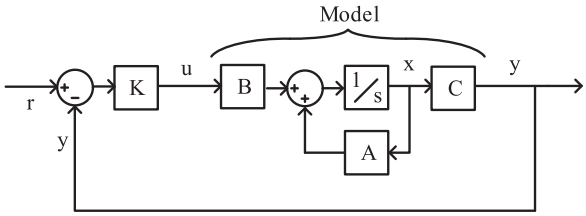

Fig. 16. Control of ac subsystem.

frequencies, but that instability may occur close to the resonant peaks.

From [48], we know that it is possible to use integral control in all of the channels of the decentralized MIMO system to achieve perfect steady-state control if and only if G(0) is nonsingular

$$\det(G(0)) = 0.0006. \tag{51}$$

The nonzero determinant (51) confirms that the G(0) matrix is nonsingular, and therefore, PI control would be suitable in all of the channels. A diagram showing the proposed closed-loop control scheme can be seen in Fig. 16.

For a converter with the parameters shown in Table I, a PI controller was designed for the loop from input v_{1d} to output i_{2q} using the previously found open-loop transfer function and MATLAB's PIDtool. The controller was designed to have no overshoot, a rise time of 4 ms and a settling time of 7 ms. The resulting controller has the following parameters:

$$k_p = 0.0006 \tag{52}$$

$$k_i = 5000. \tag{53}$$

The PI controllers for the other loops were designed using the same methodology and had the same parameters as those for the first controller due to the symmetrical nature of the CLLC network. The overall controller parameters are shown below

$$\begin{bmatrix} K_1 & 0 & 0 & 0 \\ 0 & K_2 & 0 & 0 \\ 0 & 0 & K_3 & 0 \\ 0 & 0 & 0 & K_4 \end{bmatrix} \tag{54}$$

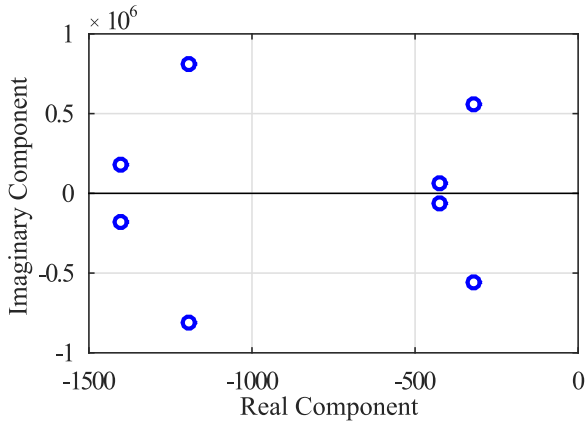

Fig. 17. Poles of the closed-loop system.

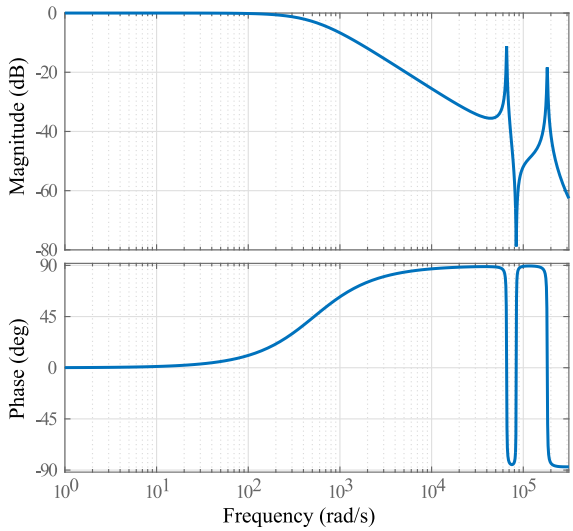

Fig. 18. Bode plot of closed-loop system.

where

$$K_3 = K_2 = -K_1 = -K_4 = k_p + \frac{k_i}{s}. \tag{55}$$

D. Closed-Loop Stability

To analyze the stability of the closed-loop system with decoupled controllers, we first have to determine that the individual loops are stable. In order to determine the stability of the individual loops, traditional SISO analysis tools will be used. In Fig. 17, the poles of the closed loop have been plotted. All the poles are on the left-hand side of the imaginary axis, and therefore, we can conclude that this loop is stable.

The bode plot of the closed loop from input v_{1d} to output i_{2q} can be seen in Fig. 18. From this figure, we can observe that the gain margin has been improved to ∞ and the gain margin is 180° within the frequency range of interest. This indicates that the response of this loop has been improved by the designed controlled.

A similar methodology was used to analyze the other loops of interest. Once the individual loops have been shown to be

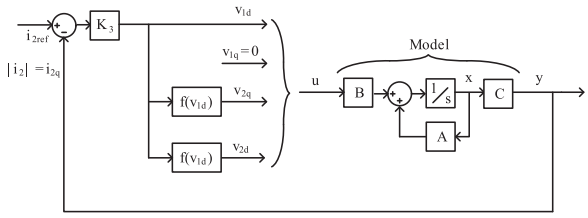

Fig. 19. Simplified controller.

stable, the overall closed-loop system has to be analyzed to ensure that the interactions between the individual closed loops do not cause instability. Using Gershgorin's theorem, we may derive sufficient conditions of overall stability in terms of rows of G

$$|\tilde{t}_i| =< |g_{ii}| / \sum_{j \neq i} |g_{ij}| \quad \forall i, \quad \forall \omega \tag{56}$$

where t_i are the diagonal elements of the complementary sensitivity function $\tilde{T}$. The sensitivity and complementary sensitivity functions are defined in

$$\tilde{S} \triangleq (I + \tilde{G}K)^{-1} \tag{57}$$

$$\tilde{T} = I - \tilde{S} \tag{58}$$

where $\tilde{G}$ for a diagonally dominant system is defined as

$$\tilde{G} \triangleq \text{diag}\{g_{ii}\} = \begin{bmatrix} g_{11} & 0 & 0 & 0 \\ 0 & g_{22} & 0 & 0 \\ 0 & 0 & \ddots & 0 \\ 0 & 0 & 0 & g_{mm} \end{bmatrix}. \tag{59}$$

For the system with the parameters shown in Table I and the controllers (52)–(55), at the frequencies of interest, the criteria of Gershgorin's theorem was met and the closed-loop system is therefore overall stable.

E. Simplified Controller

The controller shown in Fig. 16 requires the measurement of at least three output variables and the implementation of at least three PI controllers. The resulting controller is computationally intensive and measuring all the output variables at high frequencies can be challenging. This could lead to an increase in cost of the overall converter. To address this, the controller previously designed will be simplified so that only a single PI controller is necessary and only a single output variable needs to be measured.

In the previous section, it was shown that all the loops are stable whether they are open or closed. This means that even if we do not know the current value of the output variables they will eventually reach steady state if the input reference is steady. Using this knowledge, we can analyze the steady-state relationships between the inputs, u, of the system and the outputs, y, of the system and apply these relationships to our previous controller. At steady state, we have the following relationships:

TABLE II
PROTOTYPE PARAMETERS

Parameter	Value	Parameter	Value
$V_{DC1} = V_{DC2}$	20 V	f_{sw}	50 kHz
DSP Controller	F28027 Piccolo	Switches	epc2016 eGaN FETs
C_1	198 nF	L_1	50.3 μH
C_2	199 nF	L_2	50.5 μH
$R_1 = R_2$	0.04 Ω	k	0.65
Controller T_s	20 μs		

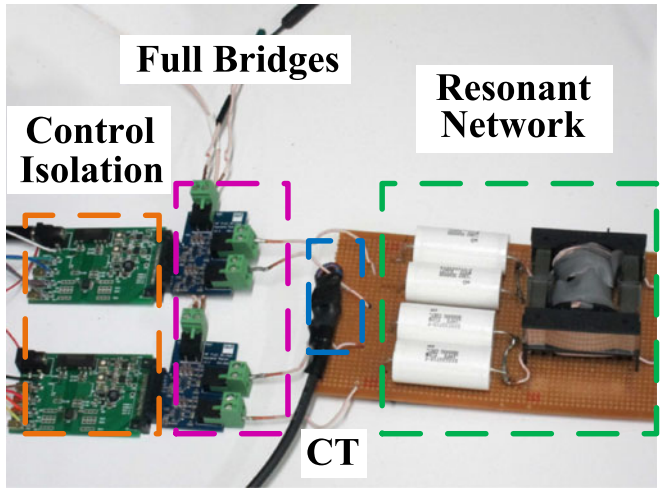

Fig. 20. Experimental prototype.

$$i_{2q} = i_{2\max} \sin(\frac{\phi_1}{2}) \tag{60}$$

$$i_{2d} = 0 \tag{61}$$

$$i_{1d} = i_{1\max} \sin(\frac{\phi_2}{2}) \sin(\theta) \tag{62}$$

$$i_{1q} = i_{1\max} \sin(\frac{\phi_2}{2}) \cos(\theta). \tag{63}$$

For the proposed modulation strategy, the relationship from (13) has to be true. Substituting this into (60)–(63)

$$i_{1d} = \frac{i_{1\max}}{i_{2\max}^2} i_{2q}^2 \tag{64}$$

$$i_{1q} = \frac{i_{1\max}}{i_{2\max}} i_{2q} \sqrt{1 - \left(\frac{i_{2q}}{i_{2\max}}\right)^2}. \tag{65}$$

And similarly v_1 can be related to v_2

$$v_{2q} = \frac{v_{1\max}}{v_{2\max}^2} v_{1d}^2 \tag{66}$$

$$v_{2d} = \frac{v_{1\max}}{v_{2\max}} v_{1d} \sqrt{1 - (\frac{v_{1d}}{v_{1\max}})^2}. \tag{67}$$

By applying these relationships to the previous controller, a new simplified controller can be derived. The simplified controller can be seen in Fig. 19. This controller only requires the

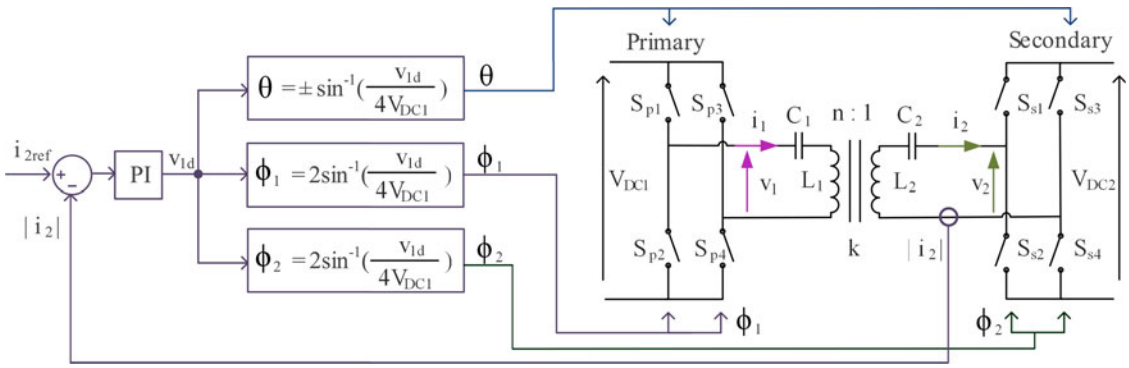

Fig. 21. Control Implementation.

measurement of i_{2q} which is the same as the amplitude of i_2, this measurement can easily be realized through the use of an inexpensive current transformer (CT). Additionally, only one PI controller is implemented with the gain K_3, the inputs for the other loops are derived from (66,67). Because this controller relies on steady-state relationships, the dynamics controlling the reference should be orders slower than the dynamics of the closed-loop system.

Before the derived controller can be implemented on a DSP, the controller will have to be discretized. Since the TPS modulation scheme is being used, we can only update the phase shifts once during every cycle of the fundamental. Therefore, the controller was converted to the discrete domain with a sampling time of 20 μs. A zero-order-hold was used to emulate the discrete behavior of the controller. The resulting controller was evaluated in MATLAB to ensure that the input to the discrete controller is not significantly impacted by aliasing, the dynamic response of the discrete controller is close to that of the continuous domain controller and that it is stable in the z-domain.

VI. Results

An experimental prototype of the CLLC RDAB, for the purpose of control validation, was built with the parameters shown in Table II. The prototype can be seen in Fig. 20. The two full-bridge converters utilize eGaN field-effect transistor (FET) and their outputs are connected through a resonant CLLC network. The current i_2 is measured by the controller through the use of a CT. The controller was implemented on a low cost F28027 Piccolo microcontroller.

The control diagram is shown in Fig. 21. The output of the PI controller is the desired value of v_{1d}, which is the required amplitude of the fundamental of v_1. This amplitude is then used to determine the necessary phase shifts, ϕ_1 and ϕ_2, so that the fundamental voltages at the outputs of the full bridges have the required magnitudes. θ is also derived from v_{1q} so that the converter remains within the soft switching range.

In Fig. 22(a)–(c), the current and voltage waveforms at the ac terminals of the primary and secondary full bridge with varying phase shifts are shown. In Fig. 22(a), both full bridges are operated at the maximum phase shift, which results in the maximum current magnitudes for both i_1 and i_2. In Fig. 22(b), the phase

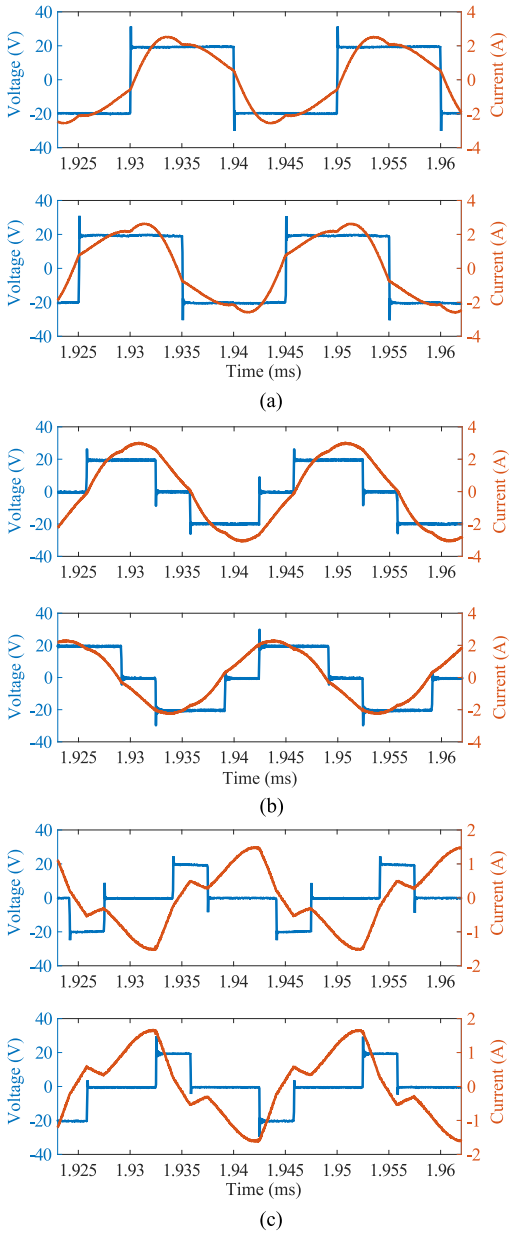

Fig. 22. Voltage and current waveforms with (a) $\phi_1 = \phi_2 = 2\theta = 180°$ (b) $\phi_1 = \phi_2 = 2\theta = 120°$ (c) $\phi_1 = \phi_2 = 2\theta = 60°$.

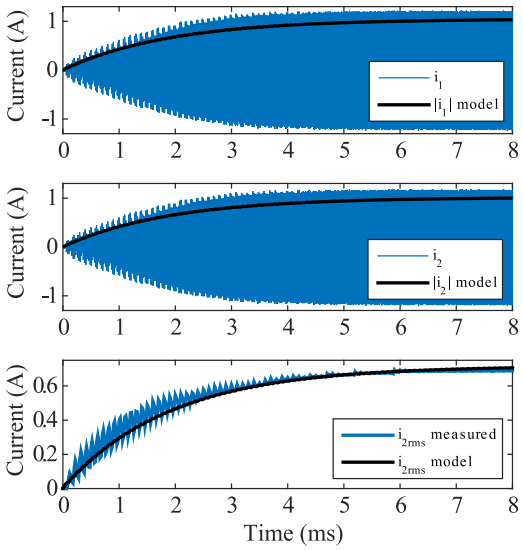

Fig. 23. Reference step of i_1 and i_2 from 0 to 2 A $t = 0$.

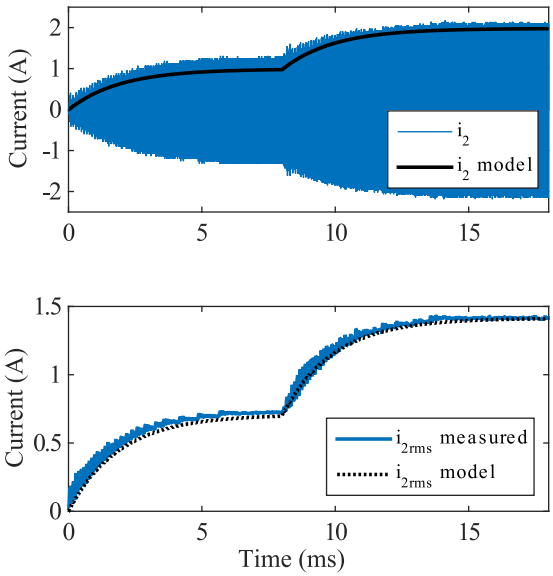

Fig. 24. Reference step of i_2 from 1 to 2 A at $t = 2$ ms.

shifts between the full-bridge legs are set to 120°, which results in the canceling of the third harmonic. In this figure, the currents at the terminals of both full bridges are closely sinusoidal. In Fig. 22(c), the converter is operated at a third of the maximum phase shift, it is apparent that there are increased levels of harmonics present in the currents. From Fig. 22(a)–(c), we can observe that all the switches in the primary full bridge are soft switching with ZVS turn-on transitions, since the current i_1 is negative on the rising edges of v_1 and is positive on the falling edges. Likewise, the soft switching in the secondary full bridge is observed by the positive current i_2 at the rising edges of v_2 and the negative current on the falling edges of v_2.

Figs. 23 and 24 show the current and voltage envelopes of i_1 and i_2 when a step is applied to the reference in the prototype compared to the predicted response by the model. The prototype waveforms are sinusoidal at the fundamental frequency

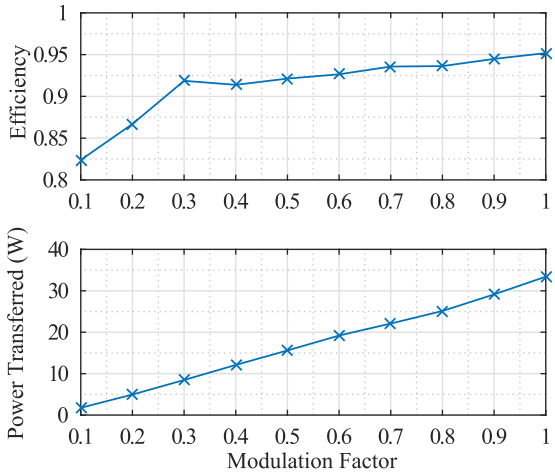

Fig. 25. Converter efficiency over the modulation range.

with some harmonic content and the model shows the predicted envelope of the currents. Since there are harmonics present in the current waveforms, the waveform amplitude is not an accurate measure of the magnitude of the fundamental component. To overcome this, the current waveform RMS was measured instead and the magnitude of the fundamental component was derived as shown in

$$|i_2| = \sqrt{2}\, i_{2\ \text{rms measured}}. \tag{68}$$

In the first figure, the reference of i_2 is set to 1 A and the startup waveform can be seen. It can be seen that there is a steady-state error between the current waveform amplitudes and that which is predicted by the model. This is expected as the harmonics in the current, which are not considered by the model, will impact the waveform amplitudes. However, as shown at the bottom of Fig. 23, the RMS of the current amplitude closely matches the response predicted by the model.

In Fig. 24, the reference for i_2 is initially set to 1 A and then at $t = 8$ ms, the reference is stepped up to 2 A. As in the previous figure, we can see that the current RMS predicted by the model closely matches that of the measured current waveform. Both the startup and step response have a rise time of 4 ms and a settle time of 7 ms which agrees with the controller that was designed earlier. It can also be seen that there are no large transients when the reference is modified, and therefore, the transformer can be designed with closer constraints on the saturation current, which could decrease the overall size and cost of the transformer while, without sacrificing the dynamic response of the converter.

The converter efficiency over the modulation range has been plotted in Fig. 25. This figure shows that the converter has a high efficiency over the modulation range even though the converter has not been optimized for efficiency.

VII. Conclusion

This paper proposed a model for an RDAB converter with a tuned CLLC network. Mathematical analysis of the RDAB converter indicated that the inputs and outputs of the MIMO system may be decoupled. The degree of coupling in the system

was further investigated by use of RGA and singular-value-decomposition (SVD) analysis which indicated that decentralized control may be suitable for the control of the CLLC RDAB converter. A dq framework was used to convert all the ac state variables into dc states with slow dynamics which are easier to control. Using the derived model, a decoupled control scheme with three PI controllers was designed to control the resonant tank currents, i_1 and i_2, and therefore, the magnitude of power transfer, while controlling the angle between the full bridges to improve the soft switching range of the converter. The controller was simplified into a single PI controller that only requires the measurement of one output variable by using steady-state relationships. The simplified PI controller was implemented in a prototype converter and it was demonstrated to be sufficient for good closed-loop dynamic response and steady-state performance. Simulation and experimental results have shown that the proposed model is useful for fast simulation, estimation of state variables under large signal variation and for closed-loop control design.

REFERENCES

[1] T. Key, "Future of renewable energy development & deployment," in *Proc. IEEE Power Energy Soc. General Meeting*, 2009, p. 1.

[2] M. H. Nazari and M. Ilic, "Potential for efficiency improvement of future electric energy systems with distributed generation units," in *Proc. IEEE Power Energy Soc. General Meeting*, 2010, pp. 1–9.

[3] R. Friedemann, F. Krismer, and J. W. Kolar, "Design of a minimum weight dual active bridge converter for an airborne wind turbine system," in *Proc. 27th Annu. IEEE Appl. Power Electron. Conf. Expo.*, 2012, pp. 509–516.

[4] F. Krismer and J. W. Kolar, "Efficiency-optimized high-current dual active bridge converter for automotive applications," *IEEE Trans. Ind. Electron.*, vol. 59, no. 7, pp. 2745–2760, Jul. 2012.

[5] S. Inoue and H. Akagi, "A bi-directional isolated dc/dc converter as a core circuit of the next-generation medium-voltage power conversion system," in *Proc. 37th IEEE Power Electron. Specialists Conf.*, 2006, pp. 1–7.

[6] F. Krismer and J. W. Kolar, "Closed form solution for minimum conduction loss modulation of dab converters," *IEEE Trans. Power Electron.*, vol. 27, no. 1, pp. 174–188, Jan. 2012.

[7] B. Zhao, Q. Song, W. Liu, and Y. Sun, "Overview of dual-active-bridge isolated bidirectional dc #x2013;dc converter for high-frequency-link power-conversion system," *IEEE Trans. Power Electron.*, vol. 29, no. 8, pp. 4091–4106, Aug. 2014.

[8] S. Inoue and H. Akagi, "A bidirectional dc–dc converter for an energy storage system with galvanic isolation," *IEEE Trans. Power Electron.*, vol. 22, no. 6, pp. 2299–2306, Nov. 2007.

[9] M. Kheraluwala, R. W. Gascoigne, D. M. Divan, and E. D. Baumann, "Performance characterization of a high-power dual active bridge dc-to-dc converter," *IEEE Trans. Ind. Appl.*, vol. 28, no. 6, pp. 1294–1301, Nov./Dec. 1992.

[10] R. W. De Doncker, D. M. Divan, and M. H. Kheraluwala, "A three-phase soft-switched high-power-density dc/dc converter for high-power applications," *IEEE Trans. Ind. Appl.*, vol. 27, no. 1, pp. 63–73, Jan./Feb. 1991.

[11] K. Wu, C. W. de Silva, and W. G. Dunford, "Stability analysis of isolated bidirectional dual active full-bridge dc–dc converter with triple phase-shift control," *IEEE Trans. Power Electron.*, vol. 27, no. 4, pp. 2007–2017, Apr. 2012.

[12] A. K. Jain and R. Ayyanar, "PWM control of dual active bridge: Comprehensive analysis and experimental verification," *IEEE Trans. Power Electron.*, vol. 26, no. 4, pp. 1215–1227, Apr. 2011.

[13] G. G. Oggier, G. O. Garcia, and A. R. Oliva, "Modulation strategy to operate the dual active bridge dc–dc converter under soft switching in the whole operating range," *IEEE Trans. Power Electron.*, vol. 26, no. 4, pp. 1228–1236, Apr. 2011.

[14] B. Zhao, Q. Song, W. Liu, and W. Sun, "Current-stress-optimized switching strategy of isolated bidirectional dc–dc converter with dual-phase-shift control," *IEEE Trans. Ind. Electron.*, vol. 60, no. 10, pp. 4458–4467, Oct. 2013.

[15] H. Zhou and A. M. Khambadkone, "Hybrid modulation for dual-active-bridge bidirectional converter with extended power range for ultracapacitor application," *IEEE Trans. Ind. Appl.*, vol. 45, no. 4, pp. 1434–1442, Jul./Aug. 2009.

[16] M. Kim, M. Rosekeit, S.-K. Sul, and R. W. De Doncker, "A dual-phase-shift control strategy for dual-active-bridge dc-dc converter in wide voltage range," in *Proc. IEEE 8th Int. Conf. Power Electron. ECCE Asia*, 2011, pp. 364–371.

[17] G. G. Oggier, G. O. Garcia, and A. R. Oliva, "Switching control strategy to minimize dual active bridge converter losses," *IEEE Trans. Power Electron.*, vol. 24, no. 7, pp. 1826–1838, Jul. 2009.

[18] W. Chen, P. Rong, and Z. Lu, "Snubberless bidirectional dc-dc converter with new CLLC resonant tank featuring minimized switching loss," *IEEE Trans. Ind. Electron.*, vol. 57, no. 9, pp. 3075–3086, Sep. 2010.

[19] F. Martin Ibanez, J. Martin Echeverria, J. Vadillo, and L. Fontan, "A step-up bidirectional series resonant dc/dc converter using a continuous current mode," *IEEE Trans. Power Electron.*, vol. 30, no. 3, pp. 1393–1402, Mar. 2015.

[20] A. K. Bhat, "Analysis and design of LCL-type series resonant converter," *IEEE Trans. Ind. Electron.*, vol. 41, no. 1, pp. 118–124, Feb. 1994.

[21] J.-H. Jung, H.-S. Kim, M.-H. Ryu, and J.-W. Baek, "Design methodology of bidirectional CLLC resonant converter for high-frequency isolation of dc distribution systems," *IEEE Trans. Power Electron.*, vol. 28, no. 4, pp. 1741–1755, Apr. 2013.

[22] H.-S. Kim, M.-H. Ryu, J.-W. Baek, and J.-H. Jung, "High-efficiency isolated bidirectional ac–dc converter for a dc distribution system," *IEEE Trans. Power Electron.*, vol. 28, no. 4, pp. 1642–1654, Apr. 2013.

[23] F. Ibanez, J. M. Echeverria, and L. Fontan, "Novel technique for bidirectional series-resonant dc/dc converter in discontinuous mode," *IET Power Electron.*, vol. 6, no. 5, pp. 1019–1028, May 2013.

[24] L. Corradini, D. Seltzer, D. Bloomquist, R. Zane, D. Maksimovic, and B. Jacobson, "Zero voltage switching technique for bidirectional dc/dc converters," *IEEE Trans. Power Electron.*, vol. 29, no. 4, pp. 1585–1594, Sep. 2014.

[25] X. Li and A. K. Bhat, "Analysis and design of high-frequency isolated dual-bridge series resonant dc/dc converter," *IEEE Trans. Power Electron.*, vol. 25, no. 4, pp. 850–862, Apr. 2010.

[26] H. Krishnaswami and N. Mohan, "Three-port series-resonant dc–dc converter to interface renewable energy sources with bidirectional load and energy storage ports," *IEEE Trans. Power Electron.*, vol. 24, no. 10, pp. 2289–2297, Oct. 2009.

[27] L. Corradini, D. Seltzer, D. Bloomquist, R. Zane, D. Maksimovic, and B. Jacobson, "Minimum current operation of bidirectional dual-bridge series resonant dc/dc converters," *IEEE Trans. Power Electron.*, vol. 27, no. 7, pp. 3266–3276, Jul. 2012.

[28] D. Jovcic and L. Zhang, "LCL dc/dc converter for dc grids," *IEEE Trans. Power Delivery.*, vol. 28, no. 4, pp. 2071–2079, Oct. 2013.

[29] J. Park and S. Choi, "Design and control of a bidirectional resonant dc–dc converter for automotive engine/battery hybrid power generators," *IEEE Trans. Power Electron.*, vol. 29, no. 7, pp. 3748–3757, Jun. 2014.

[30] J.-W. Choi and S.-K. Sul, "Resonant link bidirectional power converter. i. resonant circuit," *IEEE Trans. Power Electron.*, vol. 10, no. 4, pp. 479–484, Jul. 1995.

[31] S. Jalbrzykowski, A. Bogdan, and T. Citko, "A dual full-bridge resonant class-e bidirectional dc–dc converter," *IEEE Trans. Ind. Electron.*, vol. 58, no. 9, pp. 3879–3883, Sep. 2011.

[32] Z. U. Zahid, Z. M. Dalala, R. Chen, B. Chen, and J.-S. Lai, "Design of bidirectional dc–dc resonant converter for vehicle-to-grid (v2g) applications," *IEEE Trans. Transportation Electrification.*, vol. 1, no. 3, pp. 232–244, Oct. 2015.

[33] M. Borage, S. Tiwari, and S. Kotaiah, "Analysis and design of an LCL-t resonant converter as a constant-current power supply," *IEEE Trans. Ind. Electron.*, vol. 52, no. 6, pp. 1547–1554, Dec. 2005.

[34] M. Borage, S. Tiwari, and S. Kotaiah, "LCL-t resonant converter with clamp diodes: A novel constant-current power supply with inherent constant-voltage limit," *IEEE Trans. Ind. Electron.*, vol. 54, no. 2, pp. 741–746, Apr. 2007.

[35] M. Borage, K. Nagesh, M. Bhatia, and S. Tiwari, "Design of LCL-t resonant converter including the effect of transformer winding capacitance," *IEEE Trans. Ind. Electron.*, vol. 56, no. 5, pp. 1420–1427, May 2009.

[36] M. Borage, K. Nagesh, M. Bhatia, and S. Tiwari, "Resonant immittance converter topologies," *IEEE Trans. Ind. Electron.*, vol. 58, no. 3, pp. 971–978, Mar. 2011.

[37] R. P. Twiname, D. J. Thrimawithana, U. K. Madawala, and C. A. Baguley, "A new resonant bi-directional dc-dc converter topology," *IEEE Trans. Power Electron.*, vol. 29, no. 9, pp. 4733–4740, Sep. 2014.
[38] R. Twiname, D. Thrimawithana, U. Madawala, and C. Baguley, "A dual active bridge topology with a tuned CLC network," *IEEE Trans. Power Electron.*, vol. 30, no. 12, pp. 6543–6550, Dec. 2015.
[39] R. W. Erickson and D. Maksimovic, *Fundamentals of Power Electronics*. Norwell, MA, USA: Kluwer, 2001.
[40] P. C.-K. Luk, S. Aldhaher, W. Fei, and J. F. Whidborne, "State-space modeling of a class converter for inductive links," *IEEE Trans. Power Electron.*, vol. 30, no. 6, pp. 3242–3251, Jun. 2015.
[41] A. Swain, M. Neath, U. Madawala, and D. Thrimawithana, "A dynamic multivariable state-space model for bidirectional inductive power transfer systems," *IEEE Trans. Power Electron.*, vol. 27, no. 11, pp. 4772–4780, Nov. 2012.
[42] Z. Ye, P. Jain, and P. Sen, "Phasor-domain modeling of resonant inverters for high-frequency ac power distribution systems," *IEEE Trans. Power Electron.*, vol. 24, no. 4, pp. 911–923, Apr. 2009.
[43] A. A. Aboushady, K. H. Ahmed, S. J. Finney, and B. W. Williams, "Linearized large signal modeling, analysis, and control design of phase-controlled series-parallel resonant converters using state feedback," *IEEE Trans. Power Electron.*, vol. 28, no. 8, pp. 3896–3911, Aug. 2013.
[44] Z. Ye, P. Jain, and P. Sen, "Multiple frequency modeling of high frequency resonant inverter system," in *Proc. IEEE 35th Ann. Power Electron. Specialists Conf.*, 2004, vol. 6, pp. 4107–4113.
[45] R. Twiname, W. Malan, J. Minogue, D. Thrimawithana, U. Madawala, and C. Baguley, "A novel dual active bridge topology with a tuned CLC network," in *Proc. Int. Conf. Ind. Technol.*, Feb. 2014, pp. 1–6.
[46] E. Bristol, "On a new measure of interaction for multivariable process control," *IEEE Trans. Autom. Control.*, vol. 11, no. 1, pp. 133–134, Jan. 1966.
[47] S. Skogestad and I. Postlethwaite, *Multivariable Feedback Control: Analysis and Design*. Hoboken, NJ, USA: Wiley-Interscience, 2005, Ch. 6.8.
[48] P. J. Campo and M. Morari, "Achievable closed-loop properties of systems under decentralized control: Conditions involving the steady-state gain," *IEEE Trans. Autom. Control.*, vol. 39, no. 5, pp. 932–943, May 1994.

Wynand Louis Malan (S'12) received the B.E. (Hons.) degree in electrical engineering from University of Auckland, Auckland, New Zealand, in 2013. He is currently working toward the Ph.D. degree in power electronics at Queensland University of Technology, Brisbane, Qld., Australia.

His current research interests include the fields of power electronics, high power density converters, high switching frequency converters, and renewable energy.

D. Mahinda Vilathgamuwa (S'90–M'93–SM'99) received the B.Sc. degree in electrical engineering from the University of Moratuwa, Moratuwa, Sri Lanka, in 1985, and the Ph.D. degree in electrical engineering from Cambridge University, Cambridge, U.K., in 1993.

In 1993, he joined the School of Electrical and Electronic Engineering, Nanyang Technological University, Singapore, as a Lecturer and then became an Associate Professor. He is currently a Professor with the Queensland University of Technology, Brisbane, Australia. His current research interests include power electronic converters, electrical drives, and power quality.

Dr. Vilathgamuwa was the Chairman of the IEEE Section, Singapore, and a Member of the IEEE Industrial Electronics Society. He is an Associate Editor of the IEEE TRANSACTIONS ON INDUSTRY APPLICATIONS.

Geoffrey R. Walker (M'99) received the Ph.D. degree in multilevel converter modulation from the University of Queensland, Brisbane, Qld., Australia, in 1999.

He was the power electronics Lecturer at the University of Queensland from 1998 to 2007. From 2008 to 2013, he was a Senior Electrical Engineering Consultant in Aurecons Transmission and Distribution Group, Brisbane, across various areas including rail traction, earthing studies, electricity transmission planning, and renewable energy project design and review. He joined the Electrical Power Engineering Group, Queensland University of Technology as an Associate Professor in 2013. His current research interests include applying power electronics to applications in renewable energy (especially PV), power systems, and electric vehicles. He has also worked and maintains an active interest in the pro-audio and industrial electronics sectors.